Modelling progressive failure of fibre reinforced laminated composites: mesh objective calculations

E. J. Pineda
evan.j.pineda@nasa.gov
NASA Glenn Research Center
Cleveland, Ohio
USA

A. M. Waas
dcw@umich.edu
University of Michigan
Ann Arbor, Michigan
USA

ABSTRACT

A thermodynamically-based work potential theory for modelling progressive damage and failure in fibre-reinforced laminates is presented. The current, multiple-internal state variable (ISV) formulation, enhanced Schapery theory, utilises separate ISVs for modelling the effects of damage and failure. Damage is considered to be the effect of any structural changes in a material that manifest as pre-peak non-linearity in the stress versus strain response. Conversely, failure is taken to be the effect of the evolution of any mechanisms that results in post-peak strain softening. It is assumed, matrix microdamage is the dominant damage mechanism in continuous, fibre-reinforced, polymer matrix laminates, and its evolution is captured with a single ISV. Three additional ISVs are introduced to account for failure due to mode I transverse cracking, mode II transverse cracking, and mode I axial failure. Using the stationarity of the total work potential with respect to each ISV, a set of thermodynamically consistent evolution equations for the ISVs is derived. Typically, failure evolution (i.e. post-peak strain softening) results in pathologically mesh dependent solutions within a finite element method numerical setting. Therefore, consistent characteristic element lengths are introduced into the formulation of of the three failure potentials. The theory is implemented into commercial FEM software. The model is verified against experimental results from a laminated, quasi-isotropic, T800/3900-2 panel containing a central notch. Global load versus displacement, global load versus local strain gauge data, and macroscopic failure paths obtained from the models are compared to the experiments. Finally, a sensitivity study is performed on the failure parameters used in the model.

Paper No. 3856. Manuscript received 19 June 2012, revised version received 26 September 2012, accepted 10 October 2012.

NOMENCLATURE

D_I^f	fibre degradation parameter
D_I^m	mode I matrix degradation parameter
D_{II}^m	mode II matrix degradation parameter
$e_s(S)$	transverse matrix microdamage function
$e_{s0}, e_{s1}, e_{s2}, e_{s3}, e_{s4}, e_{s5}$	transverse matrix microdamage coefficients
E_{11}, E_{22}	Young's moduli, Pa
E_{110}	initial axial modulus, Pa
E_{220}	initial transverse modulus, Pa
E_{22}^*	damaged transverse modulus at failure initiation, Pa
E_M^j	stiffness value, Pa
$g_s(S)$	shear matrix microdamage function
$g_{s0}, g_{s1}, g_{s2}, g_{s3}, g_{s4}, g_{s5}$	shear matrix microdamage coefficients
G_{IC}^f	fibre fracture toughness, J/m^2
G_{IC}^m	mode I matrix fracture toughness, J/m^2
G_{IIC}^m	mode II matrix fracture toughness, J/m^2
G_M^j	strain energy release rate, J/m^2
G_{12}	shear modulus, Pa
G_{120}	initial shear modulus, Pa
G_{12}^*	damage shear modulus at failure initiation, Pa
k_M^j	secant stiffness of traction-separation law, J/m^2
$l_e^{(\theta+90°)}$	characteristic element length perpendicular to fiber fracture plane for fibre failure, m
$l_e^{(\theta)}$	characteristic element length perpendicular to matrix fracture plane for matrix failure, m
n_1	fracture surface normal
Q_{ij}	plane stress lamina stiffness tensor, Pa
S	dissipated potential due to matrix microdamage, Pa
S_I^f	dissipated potential due to axial fibre breakage, Pa
S_I^m	dissipated potential due to mode I matrix cracking, Pa
S_{II}^m	dissipated potential due to mode II matrix cracking, Pa
S_n	internal state variables
S_r	reduced matrix microdamage internal state variable, Pa$^{1/3}$
t_{IC}^f	fibre cohesive strength, Pa
t_{IC}^m	mode I matrix cohesive strength, Pa
t_{IIC}^m	mode II matrix cohesive strength, Pa
t_M^j	surface traction at crack tip, Pa
θ	lamina fibre orientation with respect to global co-ordinate frame, degrees
$X_{\varepsilon t}$	critical axial lamina strain
$Y_{\varepsilon C}$	critical transverse compressive lamina strain
$Y_{\varepsilon C}$	critical transverse tensile lamina strain
Z_ε	critical shear lamina strain
w_M^j	physical characteristic length of failure mechanism, m
W	elastic (recoverable) strain energy density of continuum, Pa
W_M^j	elastic (recoverable) potential due to cohesive cracks, Pa
W_E	total elastic (recoverable) potential, Pa

https://doi.org/10.1017/S0001924000007612 Published online by Cambridge University Press

W_S	total dissipated (irrecoverable) potential, Pa
W_T	total work potential, Pa
x, y, z	global Cartesian co-ordinates, Pa
x_1, x_2, x_3	local material Cartesian co-ordinates, m
δ_M^j	crack tip opening displacement, m
$\varepsilon_{11}, \varepsilon_{22}, \gamma_{12}$	lamina strains
$\varepsilon_{11}^C, \varepsilon_{22}^C, \gamma_{12}^C$	lamina strains at failure initiation
ν_{12}, ν_{21}	Poisson's ratios
f	indicates fibre field/variable
j	material index
m	indicates matrix field/variable
M	fracture mode: I, II, or III

1.0 INTRODUCTION

A thermodynamically-based, work potential theory, known as Schapery theory (ST), was developed for modelling matrix microdamage in fibre-reinforced laminates (FRLs)[1-4]. Refs 5 and 6 extended the formulation to include the effects of transverse cracking by adding an additional internal state variable (ISV) and predicted the evolution of microdamage and transverse cracking in coupon laminates analytically. Since no characteristic length was introduced into the formulation, the theory produces mesh-dependent results in a computational setting when the material enters the post-peak strain softening regime of the stress-strain response[7,8].

The ST formulation is expanded here, referred to as the enhanced Schapery theory (EST), to include the effects of macroscopic transverse and shear matrix cracking, as well as fibre breakage, using an approach that differs from[5,6,9]. A deliberate distinction between damage (pre-peak nonlinearity) and failure (post-peak nonlinearity) is elaborated upon in Section 2.2. Here, matrix microdamage is categorised as a damage mechanism, but macroscopic matrix cracking and fibre breakage are hypothesised to be failure mechanisms resulting in localisation. The traditional microdamage ISV used in ST is maintained. Upon failure initiation, the element domain is no longer considered a continuum, and a smeared crack approach is used to model the embedded discontinuities[10,11]. Three new ISVs are introduced to capture the evolution of the failure mechanisms. As with the original ST, stationarity of the total work potential with respect to each ISV is invoked to arrive at a set of evolution equations. The failure potentials, used to define the total work, are functions of the characteristic length of the finite element. Thus, energy dissipated via post-peak strain softening mechanisms is managed in a numerically objective manner.

While there are many different constitutive characterisations that can be used to model damage (pre-peak nonlinearity) in fibre reinforced laminated composites (see for example Refs 12-19), the authors have chosen ST since it leads to a characterisation that can readily incorporate coupon level test data, ideally suited to capture damage formation due to matrix cracking[6,3]. In addition, EST can also be readily incorporated into a framework that can treat post-peak softening through the crack band formulation that has been implemented at the lamina level in this paper[20] .

EST is implemented into the Abaqus finite element method (FEM) software package. Mesh objectivity was previously demonstrated in Ref. 21. In Section 3, EST is verified against experimental results for a center-notched panel (CNP). Global load versus deflection data, local strain gauge data, as well as observed failure mechanisms obtained from experiment performed at the NASA Langley Research Center (LaRC) and exhibited in Refs 22 and 23 are compared to numerical results.

https://doi.org/10.1017/S0001924000007612 Published online by Cambridge University Press

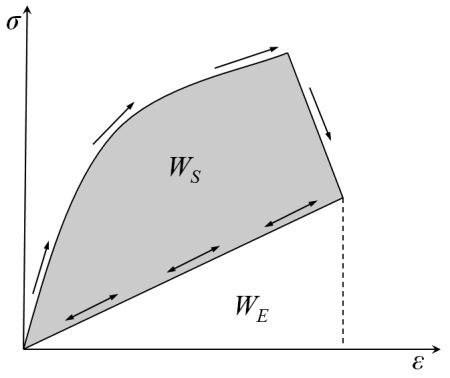

Figure 1. Typical stress-strain curve, containing pre-peak nonlinearity and post-peak strain softening, showing the total elastic (W_E) and total dissipated (W_S) potentials.

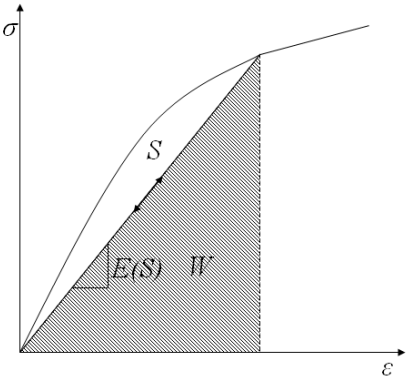

Figure 2. Typical stress-strain curve with a positive-definite tangent stiffness exhibiting microdamage, showing the elastic (W) and irrecoverable (S) portions.

2.0 ENHANCED SCHAPERY THEORY

The previously developed ST[3,24,6,25,26,9] is extended to accommodate post-peak strain softening in a numerically mesh objective fashion. Separate ISVs are used to govern the evolution of matrix microdamage, transverse (mode I) matrix failure, shear (mode II) matrix failure, and fibre breakage (mode I). The first and second laws of thermodynamics are enforced, establishing thermodynamically consistent evolution laws for progressive matrix microdamage, as well as post-peak failure.

2.1 Thermodynamically-based work potential framework

As a material is loaded, a measure of the work potential facilitates structural changes in the material, such as microcracking, which affect the elastic properties of the material. Energy that is not dissipated is recovered when the structure is unloaded. It is assumed, upon subsequent reloading, that the material behaves linearly, exhibiting the elastic properties observed during unloading, until the material reaches the preceding maximum strain state. After this state is achieved, structural changes resume, affecting the instantaneous elastic moduli of the material. This process is shown in the uniaxial stress-strain curve displayed in Fig. 1. The shaded area above the unloading line represents total dissipated potential W_S, and the triangular area underneath is the total elastic strain energy density W_E. It is assumed that the material behaves as a secant material and there is no permanent deformation upon unloading. This is a reasonable assumption for fibre-reinforced laminates[5]; however, plastic deformation can also be incorporated, if necessary[3] . Extension of ST to treat viscoelastic and viscoplastic response is outlined in Ref. 27 . A viscoplastic version of EST is currently being carried out by the authors.

The total work potential W_T can be a function of a set of ISVs, S_n, (n = 1,2, N). These account for any inelastic structural changes in the material. It is shown by Refs 2 and 3 that W_T is stationary with respect to each ISV S_n.

$$\frac{\partial W_T}{\partial S_n} = 0 \qquad \ldots (1)$$

Additionally, Ref. 28 utilised the second law of thermodynamics to establish the inequality:

https://doi.org/10.1017/S0001924000007612 Published online by Cambridge University Press

$$\dot{S}_n \geq 0 \quad \ldots (2)$$

which suggests that 'healing' is not allowed for a material undergoing structural changes. Equations (1) and (2) form the foundation of a thermodynamically-based work potential theory for modelling non-linear structural changes in a material exhibiting limited path-dependence.

2.2 Multiple ISV formulation of ST to account for multiple damage and failure mechanisms

Due to the generality of the evolution equations, Equations (1) and (2), any number of damage or failure mechanisms can be incorporated into the work potential theory. The present EST formulation assumes that three major intralaminar mechanisms are responsible for all observed non-linearities in the stress-strain curve of a composite lamina: matrix microdamage, matrix macroscopic cracking, and axial fibre failure. It should be noted that this work explicitly distinguishes between damage and failure in the following manner:

Damage Structural changes in a material that manifest as pre-peak non-linearity in the stress-strain response of the material through the degradation of the secant moduli.

Failure Structural changes that result from damage localisation in a material and manifest as post-peak strain softening in the stress-strain response of the material.

Matrix microdamage is the primary cause of observed non-linearity (i.e. systems exhibiting negligible non-linear elasticity, plasticity, or viscous effects) in the stress versus strain response of many polymer matrix composite (PMCs) laminates up to localisation of microdamage into more severe failure mechanisms, such as transverse cracking, fibre breakage, kink band formation, or delamination. Microdamage can be considered as the combination of matrix microcracking, micro-void growth, shear banding, and fiber-matrix debonding. Figure 1 shows a typical uniaxial response of a material exhibiting microdamage evolution, where the recoverable energy potential is given by W, and, the potential associated with structural changes due to microdamage is given by $S_1 = S$.

Here, three major failure mechanisms, which are distinct from the microdamage mode, are considered: transverse (mode I) matrix cracking, shear (mode II) matrix cracking, and axial (mode I) fibre fracture. These failure modes are consistent with the in-plane failure typically observed in PMC laminates. It is assumed that the evolution of these mechanisms yields an immediate reduction in the load-carrying capability of a local subvolume where the mechanisms are active. Three ISVs represent the energy potentials required to advance mode I matrix cracking, mode II matrix cracking, and mode I fibre failure, respectively: $S_2 = S_I^m$, $S_3 = S_{II}^m$, and $S_4 = S_I^f$. These ISVs are defined completely in Section 2.4.

At any given state, the total dissipated energy density W_s can be calculated as a sum of the energy potential dissipated via the aforementioned damage and failure mechanisms, given by the four ISVs.

$$W_S = S + S_I^m + S_{II}^m + S_I^f \quad \ldots (3)$$

According to the first law of thermodynamics, the total work potential (ignoring thermal dissipation) is given by the sum of the elastic strain energy density and the potentials associated with each of the damage or failure mechanisms.

$$W_T = W_E + S + S_I^m + S_{II}^m + S_I^f \quad \ldots (4)$$

https://doi.org/10.1017/S0001924000007612 Published online by Cambridge University Press

where W_E is the elastic strain energy density. Invoking the stationarity principle, Equation (1),

$$\frac{\partial W_E}{\partial S} = -1 \quad \frac{\partial W_E}{\partial S_I^m} = -1$$
$$\frac{\partial W_E}{\partial S_{II}^m} = -1 \quad \frac{\partial W_E}{\partial S_I^f} = -1 \qquad \ldots (5)$$

and the second law of thermodynamics, Equation (2), gives:

$$\dot{S} \geq 0 \quad \dot{S}_I^m \geq 0$$
$$\dot{S}_{II}^m \geq 0 \quad \dot{S}_F^f \geq 0 \qquad \ldots (6)$$

Equations (5) and (6) constitute the EST evolution equations.

2.3 Failure initiation

Matrix microdamage requires no initiation criterion. For low strain levels, the microdamage ISV remains small, and its effects on the composite moduli are not apparent. As S evolves, with increased strains, its effects on the stress-strain response of the composite become more noticeable. However, it is postulated that the evolution of the failure mechanisms immediately yield a negative tangent stiffness; therefore, initiation criteria are required. Furthermore, criteria are required to mark failure initiation because the macroscopic cracks responsible for failure may result from localisation of microdamage, or they may nucleate from pre-existing flaws in the material not necessarily associated with microdamage growth.

EST is implemented in homogenised laminae; therefore, phenomenological criteria must be employed to signal the onset of failure. Further research is needed to arrive at stability-based or micromechanics informed failure criteria for quasi-brittle PMCs. The Hashin-Rotem failure criterion incorporates separate equations for matrix failure and fibre failure initiation[29]. A local, lamina coordinate frame is chosen such that x_1,is the axial direction of the fibres, x_2 is the in-plane transverse direction, and x_3 is the out-of-plane direction. The matrix failure criterion involves contributions from both the transverse (ε_{22}) and shear (γ_{12}) strains.

$$\left(\frac{\varepsilon_{22}}{Y_{\varepsilon T}}\right)^2 + \left(\frac{\gamma_{12}}{Z_\varepsilon}\right)^2 = 1 \quad \varepsilon_{22} \geq 0$$
$$\ldots (7)$$
$$\left(\frac{\varepsilon_{22}}{Y_{\varepsilon C}}\right)^2 + \left(\frac{\gamma_{12}}{Z_\varepsilon}\right)^2 = 1 \quad \varepsilon_{22} < 0$$

where $Y_{\varepsilon T}$ is the transverse lamina failure strain in tension, $Y_{\varepsilon C}$ is the transverse failure lamina strain in compression, and Z_ε is the shear failure strain. The fibre failure criterion only involves the axial strain ε_{11};

$$\left(\frac{\varepsilon_{11}}{X_{\varepsilon T}}\right)^2 = 1 \quad \varepsilon_{11} \geq 0 \qquad \ldots (8)$$

https://doi.org/10.1017/S0001924000007612 Published online by Cambridge University Press

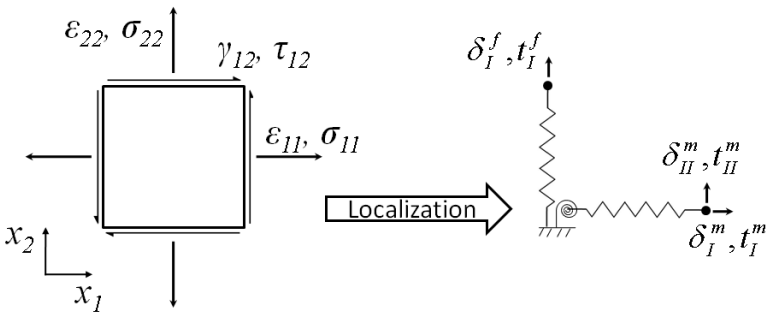

Figure 3. Schematic showing the transition form a continuum to a cohesive zone due to the initiation of macroscopic cracks. The essential, constitutive variables switch from stress and strain to traction and separation.

where $Y_{\varepsilon T}$ is the maximum allowable axial strain of the lamina. When Equation (7) is satisfied, the matrix failure ISVs S_I^m and S_{II}^m are activated, and when Equation (8) is satisfied, fibre failure evolution S_I^f is permitted; otherwise, S remains the only active ISV. Upon satisfaction of either Equation (7) or Equation (8), it is assumed that the more severe failure mechanisms dominate, superseding the effects of matrix microdamage; therefore, $S = 0$, and additional microdamage within the failed element is precluded.

2.4 Use of traction-separation relationships to define the failure potentials

It is presumed that failure arises from the evolution of cohesive cracks; however, the existence of macroscopic cracks invalidates the assumption of a continuum. The satisfaction of Equations (7) and/or Equation (8) indicates the material behavior transitions from a damaging continuum to an embedded cohesive crack. Thus, the essential fields become traction and separation, rather than stress and strain (see Fig. 3).

Following typical cohesive crack formulations[33,31], progression of the crack tip opening displacement yields a reduction in the tractions on the crack faces. If subsequently the crack is closed, it is assumed that traction at the crack tip will unload linearly towards the origin of the traction versus separa tion law (see Fig. 4). The strain energy release rate (SERR) G_M^j is calculated as:

$$G_M^j = \oint t_M^j d\delta_M^j \quad \ldots (9)$$

where j indicates the material (fibre f or matrix m), M represents the corresponding mode (Mode I or Mode II), δ_M^j is the crack tip opening displacement in mode M and material j, and t_M^j is the corresponding traction at the crack tip.

Theoretically, the shape of the traction-separation laws can take any shape without significantly affecting the FEM results[32]. For simplicity, it is assumed here that all three types of cracks obey triangular traction-separation laws, presented in Fig. 4. The total area under the traction-separation curves is controlled by the corresponding material fracture toughness in the appropriate mode, where G_{IC}^f is the mode I fracture toughness of the fibre G_{IC}^m, is the mode I fracture toughness of the matrix, and G_{IIC}^m is the mode II fracture toughness of the matrix. The cohesive strengths of the materials t_{IC}^f (mode I fibre strength), t_{IC}^m (mode I matrix strength), and t_{IIC}^m (mode II matrix

https://doi.org/10.1017/S0001924000007612 Published online by Cambridge University Press

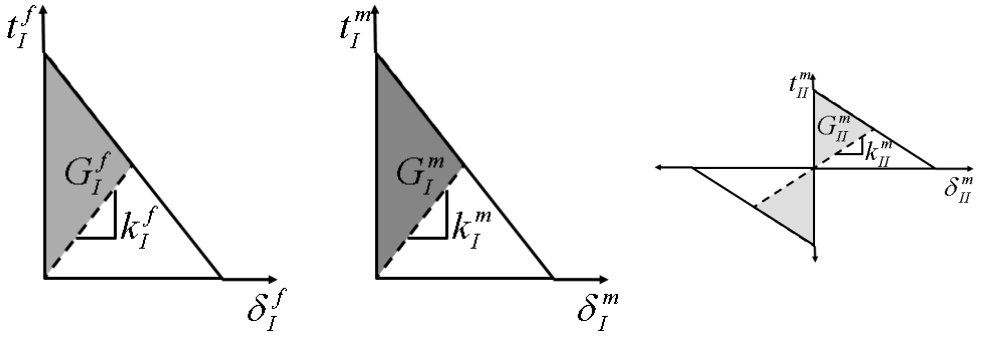

(a) Mode I fibre triangular traction separation law.

(b) Mode I matrix triangular traction separation law.

(c) Mode II matrix triangular traction separation law.

Figure 4. Triangular traction-separation laws are used to dictate the behavior of cohesive cracks embedded in the continuum. The total area under the traction-separation law represents the material fracture toughness G_{mC}^f.

strength) are given by the stresses in the continuum when Equations (7) and/or (8) are satisfied (which depends on the critical strains of the lamina). Mode I, normal cracks are not allowed to grow under compression; therefore, the mode I traction-separation laws for the fibre and matrix (Figs 4(a) and 4(b)) do not accommodate negative crack tip displacements. However under negative mode II displacement (see Fig. 4(c)), the traction on the crack faces will increase linearly until the maximum, previously attained displacement magnitude is attained. After which, the crack faces will resume unloading following the negative portion of the traction-separation law.

The traction-separation laws exhibited in Fig. 4 do not require any initial, fictitious, pre-peak stiffness because the cracks are embedded within a continuum. This is an advantage over the use of traditional cohesive elements which do require an initial, numerical stiffness. These interfacial elements do not actually represent physical material within the model and must attempt to simulate initially perfect bonding between adjacent material domains[33-36]. If set incorrectly, these fictitious stiffnesses can cause numerical problems[37,38].

Although no mode I crack can advance under compression, it is possible for post-peak softening to occur under compressive loading situations. For instance, a kink band could form under global axial compression[39,24,40], or the matrix could fail in local shear due to internal friction (Mohr-Coulomb) in quasi-brittle materials under transverse compression[31,42]. Since these failure mechanisms involve local shear at the fibre/matrix scales, which is typically below the operating lamina/laminate scale, it appears that these mechanisms evolve under mode I compression. EST could be extended further to incorporate these mechanisms through phenomenological accessions by postulating the traction-separation laws for the homogenised lamina to include the post-peak softening effects of microbuckling and Mohr-Coulomb matrix failure, accounting for energy released through these subscale failure modes. However, the examples presented in this paper are tension dominated, and extension of the theory to accommodate apparent, mode I compressive failure is left for future work.

Currently, it is assumed that the failure potentials evolve independently. However, any of the popular mixed-mode fracture theories used for cohesive zone elements could easily be implemented within EST to couple the evolution of the failure potentials [33,34,43,44].

Using the traction-separation laws in Fig. 4 and assuming the crack is not closing, the SERR

https://doi.org/10.1017/S0001924000007612 Published online by Cambridge University Press

can be calculated with Equation (9).

$$G_I^f = \frac{1}{2}\left(t_{IC}^f + t_I^f\right)\delta_I^f \quad \ldots (10)$$

$$G_I^m = \frac{1}{2}\left(t_{IC}^m + t_I^m\right)\delta_I^m \quad \ldots (11)$$

$$G_{II}^m = \frac{1}{2}\left(t_{IIC}^m + t_{II}^m\right)\delta_{II}^m \quad \ldots (12)$$

It is assumed that the energy released due to cracking is smeared over the entire element[45,10]. Thus, the failure dissipation potentials are related to the SERRs using the suitable element dimensions and removing the energy potential that may be recovered upon closing of the crack.

$$S_I^f = \frac{G_I^f}{l_e^{(\theta+90^o)}} - \frac{t_I^f \delta_I^f}{2l_e^{(\theta+90^o)}} \quad \ldots (13)$$

$$S_I^m = \frac{G_I^m}{l_e^{(\theta)}} - \frac{t_I^m \delta_I^m}{2l_e^{(\theta)}} \quad \ldots (14)$$

$$S_{II}^m = \frac{G_{II}^m}{l_e^{(\theta)}} - \frac{t_{II}^m \delta_{II}^m}{2l_e^{(\theta)}} \quad \ldots (15)$$

where $l_e^{(\theta+90^o)}$ and $l_e^{(\theta)}$ are the characteristic element lengths for fiber and matrix fracture, respectively. Schematics showing a fiber crack band and a matrix crack band are displayed in Fig. 5. The local, material frame x_1-x_2-x_3 is given with respect to the global element coordinates x-y-z, and x_1 is the local fibre direction. The normal to the fracture plane lies in the direction of the vector $\mathbf{n_1}$. When fibre failure occurs, it is assumed that the fracture plane, shown in Fig. 5, runs perpendicular to the fibre (local x_1-axis). Conversely, when matrix failure occurs (see Fig. 5), it is assumed that the crack orients parallel to the fibre direction. For an element containing a single integration point (see Fig. 5), the characteristic element length is the length of a line, perpendicular to the assumed fracture plane, intersecting two edges of an element and the element integration point. If the element contains multiple integration points, the element is partitioned into subvolumes each containing a single integration point. Then, the characteristic length is the length of a line, perpendicular to the fracture plane, intersecting the integration point and two element edges and/or subvolume boundaries. Incorporating a length scale, as such, into the ISVs results in mesh objective, post-peak, softening, as shown in Ref. 21.

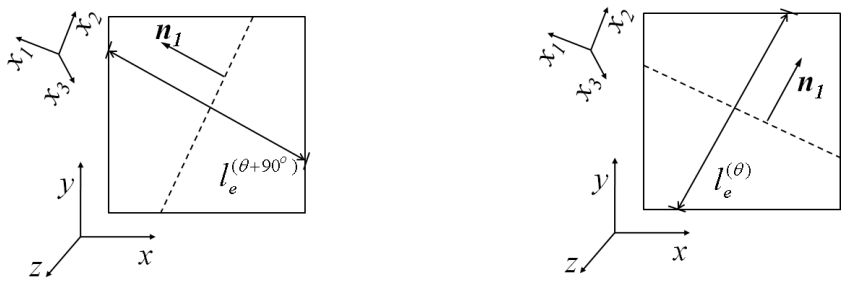

(a) fibre failure (b) matrix failure

Figure 5. Crack band orientation and characteristic length within an element, or integration point subvolume, when there is fibre failure of matrix failure.

https://doi.org/10.1017/S0001924000007612 Published online by Cambridge University Press

2.5 EST evolution equations for a fibre-reinforced lamina

To arrive at the evolution equations for the four ISVs, the elastic strain energy density must be defined for a material which may contain cohesive cracks. Therefore, the elastic strain energy W_E is comprised of a contribution from the continuum W and any possible cohesive cracks W_M^j. The plane stress, elastic strain energy density in the continuum is defined as;

$$W = \frac{1}{2}(E_{11}\varepsilon_{11}^2 + E_{22}(S)\varepsilon_{22}^2 + G_{12}(S)\gamma_{12}^2) + Q_{12}\varepsilon_{11}\varepsilon_{22} \quad \ldots (16)$$

where E_{11} is the axial elastic modulus, E_{22} is the transverse elastic modulus, G_{12} is the elastic shear modulus, $Q_{12} = E_{22}\nu_{12}$ and ν_{12} is the Poisson's ratio.

Note that only the transverse and shear module (E_{22} and G_{12}) are functions of S since matrix microdamage only accrues in the matrix, consistent with the intralaminar damage typically observed in PMC laminates. The Poisson's ratio is assumed to evolve such that the quantity $Q_{12} = E_{22}\nu_{12}$ remains constant; however, this restriction can be relaxed if deemed necessary. The degraded moduli are related to the virgin moduli (E_{220} and G_{120}) and the energy potential dissipated via matrix microdamage (S) through a set of microdamage functions ($e_s(S)$ and $g_s(S)$).

$$E_{22} = E_{220}e_s(S) \quad \ldots (17)$$

$$G_{12} = G_{120}g_s(S) \quad \ldots (18)$$

These functions are obtained from the stress-strain response of three uniaxial coupon tests[2,5,6]. For each time point, a total energy potential is calculated and partitioned into recoverable and dissipated portions. Likewise, the corresponding, degraded transverse and shear moduli can be calculated and normalised by the initial values. This data is then fit with a polynomial curves to arrive at $e_s(S)$ and $g_s(S)$.

The elastic strain energy density of the cohesive cracks are postulated as the recoverable energy per unit crack surface area smeared over the entire element.

$$W_I^f = \frac{t_I^f \delta_I^f}{2l_e^{(\theta+90^\circ)}} \quad \ldots (19)$$

$$W_I^m = \frac{t_I^m \delta_I^m}{2l_e^{(\theta)}} \quad \ldots (20)$$

$$W_{II}^m = \frac{t_{II}^m \delta_{II}^m}{2l_e^{(\theta)}} \quad \ldots (21)$$

The tractions in Equations (19)-(21) can be related to the corresponding crack tip opening displacements with secant stiffnesses from the traction-separation laws k_M^j.

$$t_I^f = k_I^f \delta_I^f \quad \ldots (22)$$

$$t_I^m = k_I^m \delta_I^m \quad \ldots (23)$$

https://doi.org/10.1017/S0001924000007612 Published online by Cambridge University Press

$$t_{II}^{m} = k_{II}^{m}\delta_{II}^{m} \quad \ldots (24)$$

Hence, the total elastic strain energy density in the continuum is given by;

$$W_E = \frac{1}{2}\left(E_{11}\varepsilon_{11}^2 + E_{22}(S)\varepsilon_{22}^2 + G_{12}(S)\gamma_{12}^2\right) + Q_{12}\varepsilon_{11}\varepsilon_{22} + \frac{k_I^f(S_I^f)}{2l_e^{(\theta+90^\circ)}}\delta_I^{f2} + \frac{k_I^m(S_I^m)}{2l_e^{(\theta)}}\delta_I^{m2} + \frac{k_{II}^m(S_{II}^m)}{2l_e^{(\theta)}}\delta_{II}^{m2} \quad \ldots (25)$$

Substituting Equation (25) into Equations (5) gives the ISV evolution equations.

$$\frac{1}{2}\left(\varepsilon_{22}^2 E_{220}\frac{\mathrm{d}e_s}{\mathrm{d}S_r} + \gamma_{12}^2 G_{120}\frac{\mathrm{d}g_s}{\mathrm{d}S_r}\right) = -3S_r^2 \quad \ldots (26)$$

$$\frac{1}{2l_e^{(\theta+90^\circ)}}\frac{\mathrm{d}k_I^f}{\mathrm{d}S_I^f}\delta_I^{f2} = -1 \quad \ldots (27)$$

$$\frac{1}{2l_e^{(\theta)}}\frac{\mathrm{d}k_I^m}{\mathrm{d}S_I^m}\delta_I^{m2} = -1 \quad \ldots (28)$$

$$\frac{1}{2l_e^{(\theta)}}\frac{\mathrm{d}k_{II}^m}{\mathrm{d}S_{II}^m}\delta_{II}^{m2} = -1 \quad \ldots (29)$$

The use of a reduced ISV $S_r = S^{1/3}$ has been employed in Equation (26)[5]. Reference 5 has shown that the use of this reduced ISV yields polynomial forms of the microdamage functions in Equations (17) and (18). Using the chain rule and the fact that;

$$\frac{\mathrm{d}S_I^f}{\mathrm{d}\delta_I^f} = \frac{t_{IC}^f}{2l_e^{(\theta+90^\circ)}} \quad \ldots (30)$$

$$\frac{\mathrm{d}S_I^m}{\mathrm{d}\delta_I^m} = \frac{t_{IC}^m}{2l_e^{(\theta)}} \quad \ldots (31)$$

$$\frac{\mathrm{d}S_{II}^m}{\mathrm{d}\delta_{II}^m} = \frac{t_{IIC}^m}{2l_e^{(\theta)}} \quad \ldots (32)$$

from Equations (10)-(15), the cohesive secant stiffnesses are determined.

$$k_I^f = -\int \frac{t_{IC}^f}{\delta_I^{f2}}\mathrm{d}\delta_I^f \quad \ldots (33)$$

https://doi.org/10.1017/S0001924000007612 Published online by Cambridge University Press

$$k_I^m = -\int \frac{t_{IC}^m}{\delta_I^{m\,2}}\,\mathrm{d}\delta_I^m \qquad \ldots (34)$$

$$k_{II}^m = -\int \frac{t_{IIC}^m}{\delta_{II}^{m\,2}}\,\mathrm{d}\delta_{II}^m \qquad \ldots (35)$$

Evaluating the integrals in Equations (33)-(35), while enforcing $k_M^j = 0$ when $\delta_M^j = \frac{2G_{MC}^j}{t_{MC}^j}$ results in expressions for k_M^j in terms of δ_M^j.

$$k_I^f = t_{IC}^f\left(\frac{1}{\delta_I^f} - \frac{t_{IC}^f}{2G_{IC}^f}\right) \qquad \ldots (36)$$

$$k_I^m = t_{IC}^m\left(\frac{1}{\delta_I^m} - \frac{t_{IC}^m}{2G_{IC}^m}\right) \qquad \ldots (37)$$

$$k_{II}^m = t_{IIC}^m\left(\frac{1}{\delta_{II}^m} - \frac{t_{IIC}^m}{2G_{IIC}^m}\right) \qquad \ldots (38)$$

The thermodynamically consistent stiffnesses derived in Equations (36)-(38) can also be derived directly from the traction-separation laws using geometry.

Finally, it is assumed that following failure initiation the strains are related to the crack tip opening displacements by;

$$l_e^{(\theta+90^\circ)}\varepsilon_{11} = l_e^{(\theta+90^\circ)}\varepsilon_{11}^C + \delta_I^f \qquad \ldots (39)$$

$$l_e^{(\theta)}\varepsilon_{22} = l_e^{(\theta)}\varepsilon_{22}^C + \delta_I^m \qquad \ldots (40)$$

$$l_e^{(\theta)}\gamma_{12} = l_e^{(\theta)}\gamma_{12}^C + 2\delta_{II}^m \qquad \ldots (41)$$

where ε_{11}^C, ε_{22}^C, and γ_{12}^C are the strains when Equations (7) and/or (8) are satisfied. Equations (39)-(41) imply that the strain in the continuum remains at the values obtained when failure initiates, and that any incremental change in the global strain after failure initiation is used wholly to advance the crack tip opening displacement. To account for changes in the continuum strain after failure initiates, it can be assumed that the stress state in the cracked body is homogenous and the tractions on the crack tip faces are equal to the stresses in the continuum[46]. Then, the strains in Equation (25) can be formulated in terms of the cohesive secant stiffnesses and the crack tip opening displacement. However, it is assumed that the evolution of strain in the continuum is negligible once cohesive cracks form.

Equations (39)-(41) can be utilised in Equations (36)-(38) to obtain k_M^j as functions of the global strain at an integration point.

$$k_I^f = t_{IC}^f\left[\frac{1}{l_e^{(\theta+90^\circ)}\left(\varepsilon_{11} - \varepsilon_{11}^C\right)} - \frac{t_{IC}^f}{2G_{IC}^f}\right] \qquad \ldots (42)$$

https://doi.org/10.1017/S0001924000007612 Published online by Cambridge University Press

$$k_I^m = t_{IC}^m \left[\frac{1}{l_e^{(\theta)} \left(\varepsilon_{22} - \varepsilon_{22}^C \right)} - \frac{t_{IC}^m}{2G_{IC}^m} \right] \quad \ldots (43)$$

$$k_{II}^m = t_{IIC}^m \left[\frac{2}{l_e^{(\theta)} \left(\gamma_{12} - \gamma_{12}^C \right)} - \frac{t_{IIC}^m}{2G_{IIC}^m} \right] \quad \ldots (44)$$

Once failure initiates, it supersedes the effects of microdamage and evolution of S ceases, within that element. Then, the axial,transverse, and shear moduli of the element can be calculated using Ref. 10;

$$E_{11} = \frac{E_{110} t_{IC}^f \left[1 + \frac{l_e^{(\theta+90^\circ)} t_{IC}^f}{2G_{IC}^f} \left(\varepsilon_{11} - \varepsilon_{11}^C \right) \right]}{1 - E_{110} \left(\varepsilon_{11} - \varepsilon_{11}^C \right)} \quad \ldots (45)$$

$$E_{22} = \frac{E_{22}^* t_{IC}^m \left[1 + \frac{l_e^{(\theta)} t_{IC}^m}{2G_{IC}^m} \left(\varepsilon_{22} - \varepsilon_{22}^C \right) \right]}{1 - E_{22}^* \left(\varepsilon_{22} - \varepsilon_{22}^C \right)} \quad \ldots (46)$$

$$G_{12} = \frac{G_{12}^* 2 t_{IIC}^m \left[1 + \frac{l_e^{(\theta)} t_{IIC}^m}{4G_{IIC}^m} \left(\gamma_{12} - \gamma_{12}^C \right) \right]}{1 - G_{12}^* \left(\gamma_{12} - \gamma_{12}^C \right)} \quad \ldots (47)$$

where E_{22}^* and G_{12}^* are the degraded transverse and shear moduli, due to microdamage, when Equation (7) is satisfied.

For visualisation purposes in the FEM simulations, degradation parameters are defined which relate the current, degraded stiffnesses to their original values upon failure initiation.

$$D_I^f = 1 - \frac{E_{11}}{E_{11}^*} \quad \ldots (48)$$

$$D_I^m = 1 - \frac{E_{22}}{E_{22}^*} \quad \ldots (49)$$

$$D_{II}^m = 1 - \frac{G_{12}}{G_{12}^*} \quad \ldots (50)$$

The negative tangent stiffness of the stress-strain curve necessary for post-peak strain softening to occur restricts the maximum allowable element size, as shown by Ref. 10.

https://doi.org/10.1017/S0001924000007612 Published online by Cambridge University Press

$$l_e^{(\theta+90^\circ)} < \frac{2G_{IC}^f E_{11}}{t_{IC}^{f\,2}} \quad \ldots (51)$$

$$l_e^{(\theta)} < \min\left\{\frac{2G_{IC}^m E_{22}^*}{t_{IC}^{m\,2}}, \frac{2G_{IIC}^m G_{12}^*}{t_{IIC}^{m\,2}}\right\} \quad \ldots (52)$$

The analyst must be careful to ensure the dimensions of any failing elements are smaller than the conditions given in Equations (51)-(52); otherwise, the response will exhibit non-physical snap-back.

In summary, Equations (7) and (8) mark the transition from evolving microdamage to failure to macroscopic cracking. Prior to failure initiation, Equation (26) is used to calculate the microdamage reduced ISV S_r, and the failure ISVs S_I^f, S_I^m and S_{II}^m remain zero. Equations (17) and (18) are used to calculate the degraded transverse and shear moduli. Subsequent to failure initiation, microdamage growth precluded, and S_r remains at S_r^*: the value of S_r when Equation (7) was satisfied. The degeneration of the transverse and shear moduli, resulting from matrix transverse and shear cracking, is calculated using Equations (46) and (47). Finally if Equation (8) is satisfied, the axial modulus is calculated using Equation (45) as fibre breakage evolves in the element. Once the material moduli have been calculated using the appropriate evolution equations, the stresses can be updated accordingly.

3.0 EXAMPLE – CENTRE NOTCHED PANEL SUBJECTED TO UNIAXIAL TENSION

3.1 Experimental details

A center-notched panel (CNP) was tested at the NASA Langley Research Center (LaRC)[22,23]. The panel was comprised of laminated T800/3900-2 carbon fibre/toughened epoxy composite. The

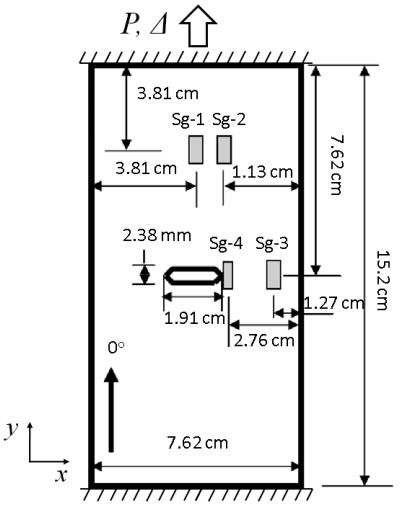

Figure 6. Geometry, boundary conditions, and strain gauge (Sg) locations of CNPs tested at NASA LaRC[22].

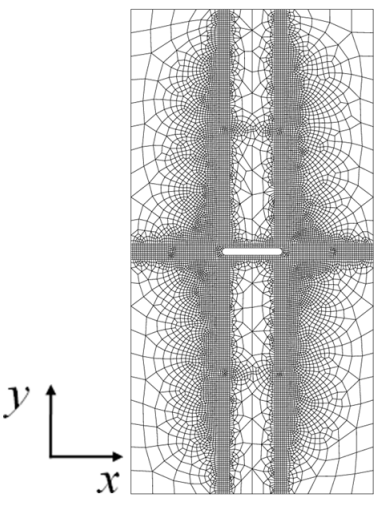

Figure 7. Finite element mesh used to simulate tensile loading of CNPs.

https://doi.org/10.1017/S0001924000007612 Published online by Cambridge University Press

quasi-isotropic stacking sequence for the panel was $(45°/0°/–45°/0°/90°)_s$. The geometrical details of the panel and testing boundary conditions are presented in Fig. 6. The 7·62cm × 15·2cm panel contained a centrally located notch that was 1·91cm wide and had a notch tip radius of 2·38mm. The end tabs were clamped and a uniform, vertical, tensile displacement (in the y-direction) was applied to the top edge. The bottom edge was fixed, preventing any y-displacement. The gripped edges also prevented any displacement in the x-direction at the top and bottom boundaries.

Several strain gauges where affixed to the test panel, labeled Sg-1 through Sg-4 in Fig. 6. Displacement measurements were taken from a 10·2cm gauge section of the specimen using extensometers. Global load versus displacement data (of the 10·2cm section), and local strain gauge data was reported in Refs 22 and 23, along with a post-test photograph of the failed specimen.

3.2 Finite element model details

The finite element mesh, containing linear, plane stress, quadrilateral, S4R Abaqus[47] shell elements, used to model the panels is displayed in Fig. 7. This mesh was obtained by refining a coarse mesh utilising observations from preliminary simulations. Nodal displacements and rotations were applied/prohibitted at the top and bottom edges of the domain to simulate the boundary conditions in the experiment.

Table 1
Linear elastic properties for T800/3900-2 used in FEM models

Property	T800/3900-2
E_{11} (GPa)	160·0
E_{22} (GPa)	8·96
G_{12} (GPa)	6·21
v_{12}	0·28

The linear elastic properties of T800/3900-2 used in the FEM model are presented in Table 1, and were taken from Ref. 22. The shear microdamage function g_s utilised in Equation (18) was obtained from $(45°/–45°)_{3S}$ angle-ply T800/3900-2 coupon tests. The transverse, tensile and compressive microdamage functions were inferred by scaling the coefficients of the microdamage curves presented by Ref. 5 for AS4/3502, as the stress-strain curves of the coupon laminates necessary to characterise were not available. The ratio of the virgin transverse modulus of T800/3900-2 to that of AS4/3502 was used as the scaling factor[48]. The polynomial forms of e_s

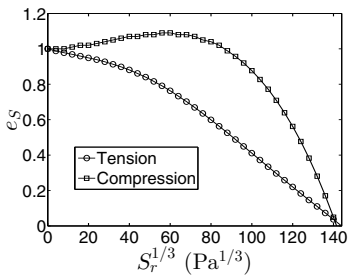

(a) Shear microdamage function obtained from ±45 angle-ply laminate

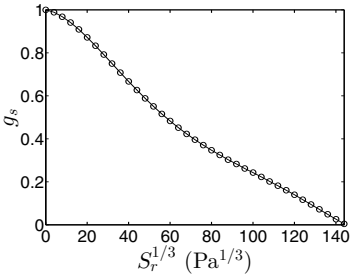

(b) Transverse tension and compression microdamage functions obtained by scaling data for AS4/3502 in Ref. 5

Figure 8. Microdamage functions for T800/3900-2 used in FEM models.

https://doi.org/10.1017/S0001924000007612 Published online by Cambridge University Press

and g_s are

$$e_s(S_r) = e_{s0} + e_{s1}S_r + e_{s2}S_r^2 + e_{s3}S_r^3 + e_{s4}S_r^4 + e_{s5}S_r^5 \quad \ldots (53)$$

$$g_s(S_r) = g_{s0} + g_{s1}S_r + g_{s2}S_r^2 + g_{s3}S_r^3 + g_{s4}S_r^4 + g_{s5}S_r^5 \quad \ldots (54)$$

The microdamage curves are plotted in Fig. 8.

The axial mode I, transverse mode I, and shear mode II critical cohesive strains, and fracture toughnesses are given in Table 2. The matrix mode I and mode II cohesive critical strains ($Y_{\varepsilon T}$, $Y_{\varepsilon C}$, and Z_ε) and the fracture toughnesses (G^m_{IC} and G^m_{IIC}) were calibrated using data from a (0°) CNP given in Ref. 22.

Table 2
Failure parameters for T800/3900-2

Critical Strain		Fracture Toughness	
$X_{\varepsilon T}$	0·021	G^f_{IC}	179kJ/mm^2
$Y_{\varepsilon T}$	0·0092	G^m_{IC}	4·19kJ/mm^2
$Y_{\varepsilon C}$	0·0115		
Z	0·0075	G^m_{IIC}	1·19kJ/mm^2

3.3 Results

Numerical results for applied load versus displacement are presented in Fig. 9. The experimental ultimate load 68·1kN correlates well (axial failure parameters were calibrated to obtain an ultimate load that most closely matched the experimental data) with the ultimate load obtained from the model 66·8kN The global response up to failure is nearly linear and failure occurs suddenly and catastrophically.

Figure 10 compares the applied load versus strain gauge results from the model to the data from the experiment. Sg-1 and Sg-2 exhibited similar behavior; the strain increases until the ultimate load is obtained, after which the strain relaxes abruptly. The experimental data and numerical results both display this behavior. The model exhibits slightly more strain, for a given load, prior to ultimate failure. At Sg-3, the model predicts strain localisation after the ultimate load is achieved. The gauge data shows a slight reduction in strain as the load drops; however, the gauge was placed directly in the crack path and may have been damaged when the panel failed. The model results and experimental data for Sg-4 exhibit similar trends, but the strain gauge shows a large degree of nonlinearity at the notch tip. Reference 22 attributed this observed nonlinearity to local interlaminar stresses near the notch free edge which caused some local

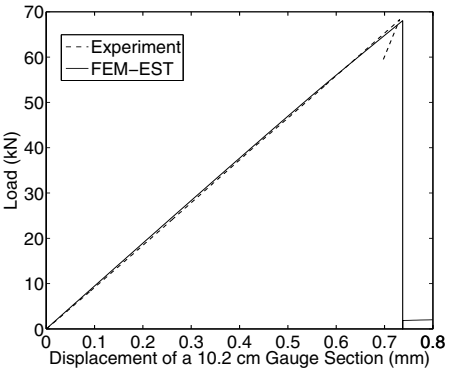

Figure 9. Applied load versus displacement of a 10·2cm section of the panel.

https://doi.org/10.1017/S0001924000007612 Published online by Cambridge University Press

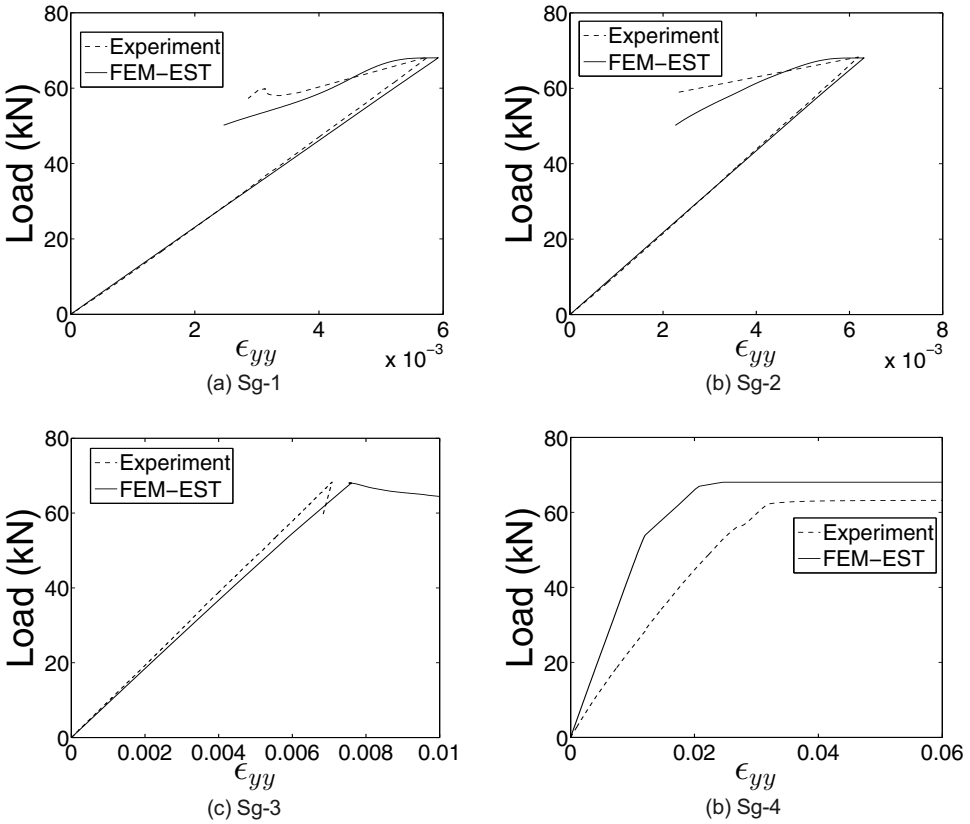

Figure 10. Applied load versus local strain.

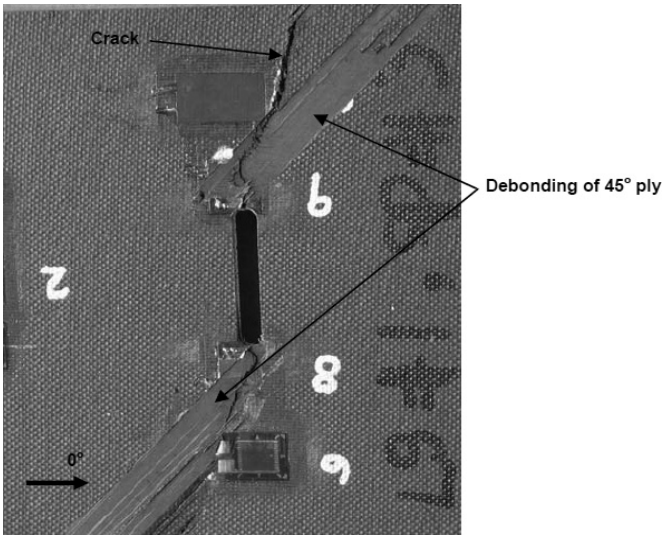

Figure 11. Photograph of failed specimen[22].

https://doi.org/10.1017/S0001924000007612 Published online by Cambridge University Press

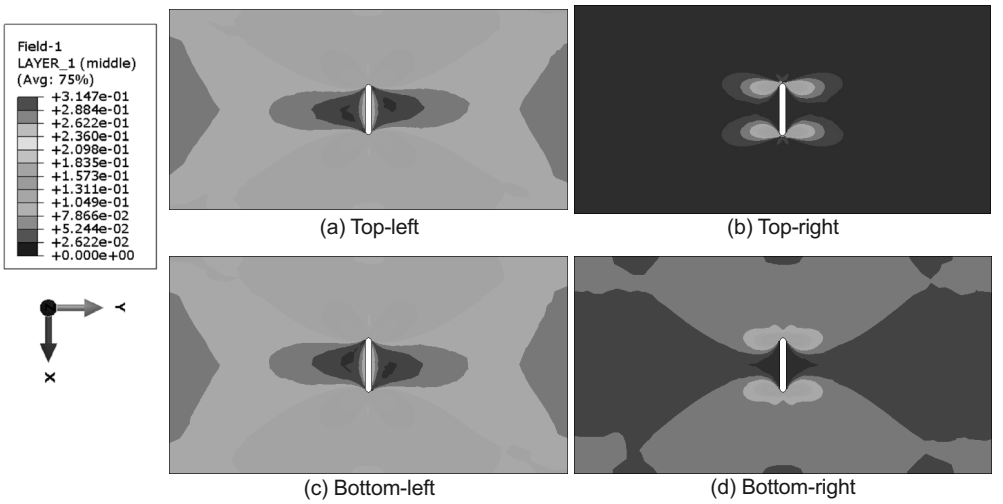

Figure 12. Normalised matrix microdamage contour S_r/S_r^{max} just prior to first axial failure initiation P = 38·4kN.

delaminations. Since the focus of this work was modelling in-plane damage mechanisms, these effects are not captured; however, the model could be easily extended to incorporate delamination by placing cohesive elements between continuum shell layers[23].

In the experiment, the gauges measure the strain over a continuous area associated with the size of the gauge, but in the model, the strain is taken at the integration point of an element; thus, these measures should not be expected to correspond exactly. In areas where there are large gradients present, such as near a notch tip (Sg-4) or near cracks, it becomes even more difficult to relate the strain gauge data to numerical strains from a discretised continuum. This may contribute to some of the discrepancies between the local gauge data and the model results in Fig. 10.

A photograph taken of the failed specimen is presented in Fig. 11. The photograph shows that two macroscopic cracks initially propagate from the notch tip towards the free edges, perpendicular to the applied load, in a self-similar fashion; i.e. the normal to the macroscopic fracture plane does not change. Eventually, the cracks turn and proceed towards the free edge at an angle. Reference 22 claim, supported by visual image correlation displacement data, that there was some eccentricity in the specimen alignment, which resulted in deviation from self-similar crack growth.

Normalised microdamage contours just prior to the ultimate load are presented for the outermost 45°, 0°, –45° , and 90° plies in Fig. 12. Similar microdamage patterns are evident in the 45° and –45° layers. Microdamage propagates outward, toward the free edge, from the notch tip in petal-like patterns. The microdamage in these layers is highly distributed throughout the plies. The 0° ply displays a more contained microdamage pattern associated with axial splitting. A moderate level of microdamage is also displayed in the 90° layer, but a low degree of microdamage is distributed throughout most of the layer.

Figure 13 shows the axial failure degradation parameter D_1^f at the ultimate load for the outer 45° and 0° layers. A small amount of axial failure in the 45° and 0° layers can be observed at the notch tips. It appears that more failure occurs at one notch tip than the other. This can be attributed to numerical imperfections resulting from dissimilar meshes at the opposite notch tips, that is the mesh is not symmetric about the y-axis. The axial failure in the –45° layer resembled that in the 45° layer, and no axial failure was observed in the 90° ply.

https://doi.org/10.1017/S0001924000007612 Published online by Cambridge University Press

Contours of the transverse, mode I, failure degradation parameter D_I^m in the outer 45° and 90° layers at the ultimate load are plotted in Fig. 14. The failure patterns were similar in the 45° and –45° plies and are comparable to the microdamage contours in Figs 12(a) and 12(c), except no failure is present directly above or below the notch. Furthermore, small, highly degraded domains can be observed propagating from the notch tip at an angle corresponding to the fibre direction in the ply. The 90° layer exhibits some moderate degradation in a localised region around the notch tips. The 0° layer did not exhibit much transverse cracking. Contours of the shear, mode II, failure degradation parameterare presented at the ultimate load in Fig. 15. Very similar failure paths can be seen in the 45° and –45° layers and the patterns are nearly symmetric across both centerlines of the panel. This is expected because as Fig. 4 indicates, the sign of the local shear strain does not affect the failure degradation D_{II}^m in the 0° and 90° is limited to very small regions surrounding the notch tips.

Contours representing the microdamage in the four unique layers are presented in Fig. 16 after the panel has completely failed and lost all of its load carrying capability. Although further matrix microdamage evolution is prohibited in elements that have failed (transverse/shear or axial), in the elements that have not failed, matrix microdamage evolution continues. Nearly the entire 45° and –45° layers reach a microdamage level of 0·18 S_r^{max}. The 0° and 90° plies exhibit similar

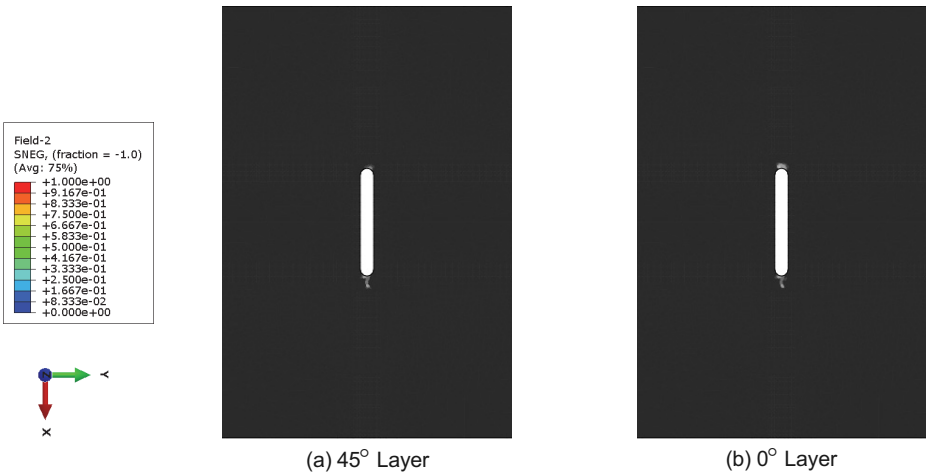

(a) 45° Layer (b) 0° Layer

Figure 13. Fibre failure degradation D_I^f at ultimate load P = 66·8kN (magnified view of region near notch).

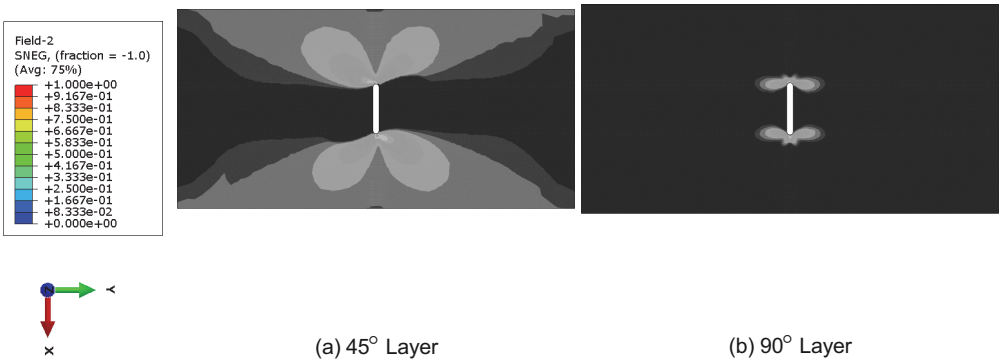

(a) 45° Layer (b) 90° Layer

Figure 14. Transverse matrix failure degradation D_I^m at ultimate load P = 66·8kN.

https://doi.org/10.1017/S0001924000007612 Published online by Cambridge University Press

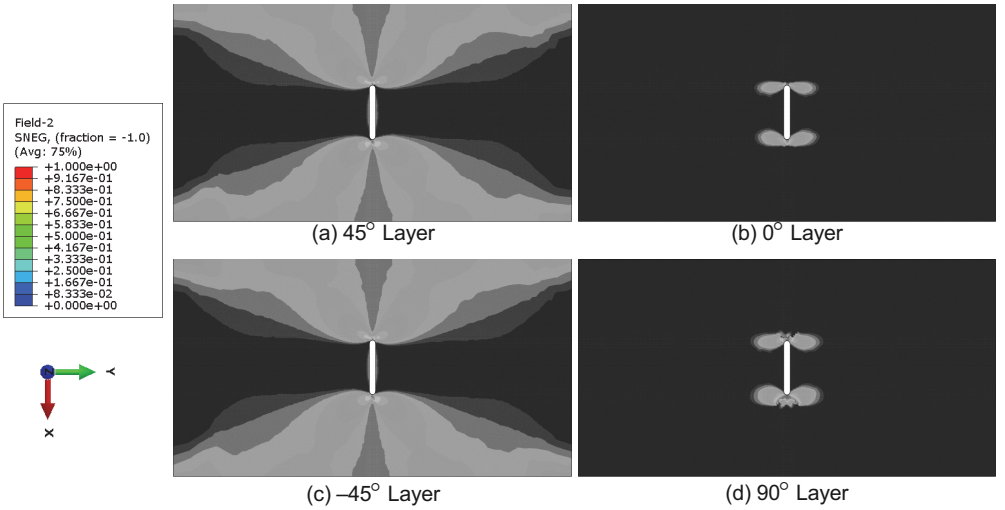

Figure 15. Shear matrix failure degradation D_{II}^{m} at ultimate load P = 66·8kN.

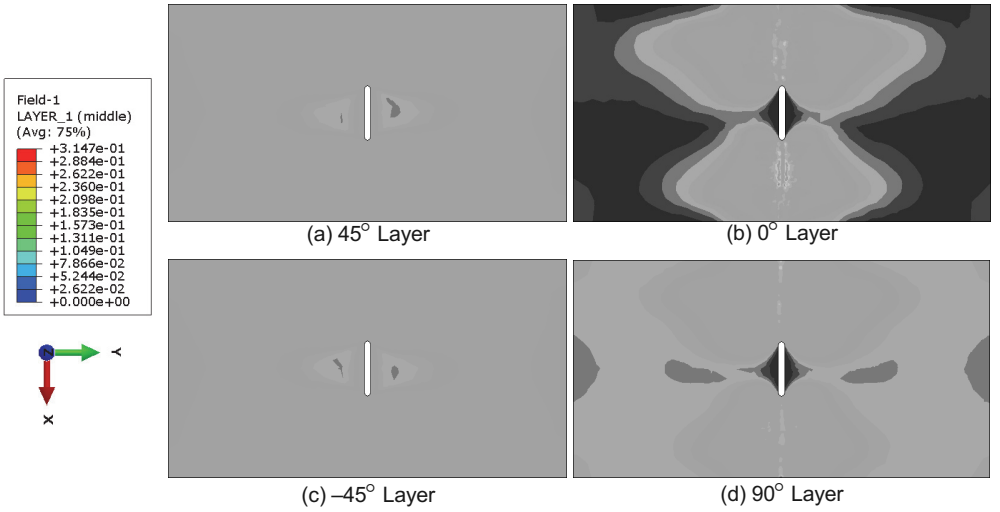

Figure 16. Normalised matrix microdamage contour S_r/S_r^{max} after specimen has lost load carrying capability.

microdamage patterns; however, low levels of microdamage are more widespread in the 90° ply.

Figure 17 shows the fibre failure path once the specimen has completely failed. Both the 0° and 45° layers show self similar cracks propagating from the notch tips towards the free edges of the panel. The –45° ply (not shown) also exhibited this, but the 90° layer did display any fibre failure. The angled crack path shown in Fig. 10 was not reproduced because the eccentric loading (suspected in the test) was not introduced into the simulation; therefore, the crack growth remained self-similar.

A high degree of transverse matrix failure can be seen in the axial crack path in the 45° and 90° plies in Fig. 18. Finally, D_{II}^{m} is presented after the specimen has failed in Fig. 19. Similar failure to Figs 15(a) and 15(c) in the 45° and –45° is exhibited, but a highly degraded region has localised in the axial crack path. Figures 9(b) and 9(d) show fairly extensive regions containing a high degree of shear matrix failure surrounding the axial failure path.

https://doi.org/10.1017/S0001924000007612 Published online by Cambridge University Press

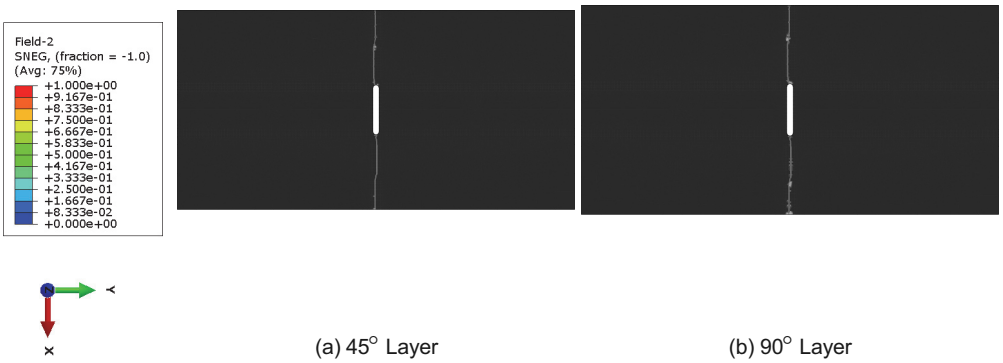

(a) 45° Layer (b) 90° Layer

Figure 17. Fibre failure degradation D_I^f after specimen has lost load carrying capability.

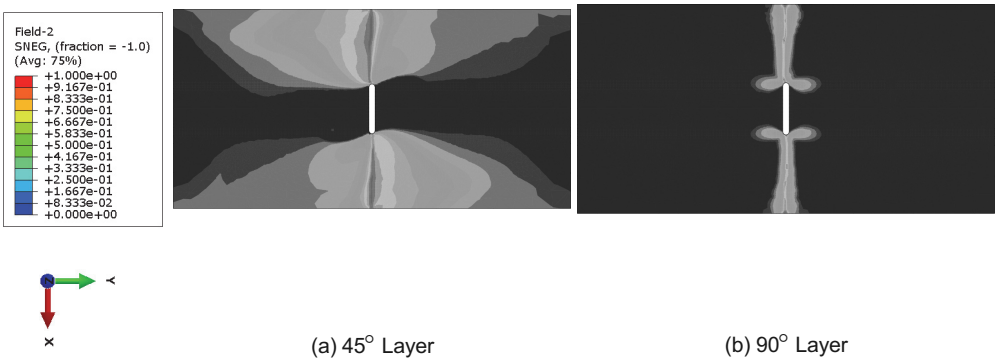

(a) 45° Layer (b) 90° Layer

Figure 18. Transverse matrix failure degradation D^m_I after specimen has lost load carrying capability.

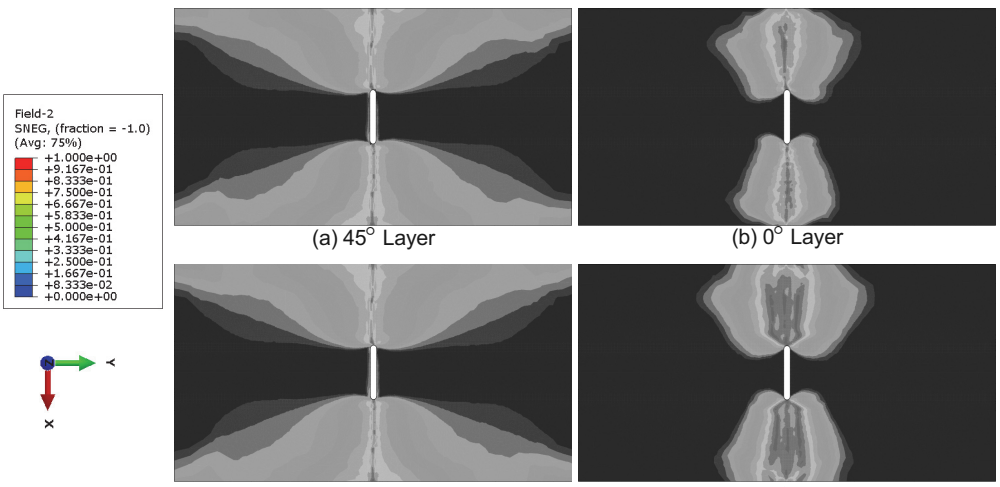

(a) 45° Layer (b) 0° Layer

(c) –45° Layer (d) 90° Layer

Figure 19. Shear matrix failure degradation D^m_{II} after specimen has lost load carrying capability.

https://doi.org/10.1017/S0001924000007612 Published online by Cambridge University Press

3.4 Sensitivity to failure parameters

Due to limited experimental data, the failure parameters used in the simulation (given in Table 2) where calibrated to the results from (0°) and (45°/0°/–45°/0°/90°)s CNPs, rather than being measured directly from experiments. The (0°) laminate did not exhibit any axial failure; so, the fibre mode I parameters ($X_{\varepsilon T}$ and G_{IC}^{f}) were calibrated such that the ultimate load from the simulation of the quasi-isotropic laminate corresponded with the ultimate load reported by Ref. 22. The shear failure strain and mode II fracture toughness were calibrated such that the splitting load from a simulation of the (0°) CNP correlated with the experiment. The splitting load was considered as the load at which the axial strain reverses in the strain gauge located far above the notch in the center of the panel (Sg-1) and was measured to be 36·7kN[22]. The critical transverse strain was estimated using the ratio of the transverse strengths of IM7/8552[49] to the calibrated T800/3900-2 critical shear strain.

The characteristic length of the failure mechanism can be calculated[10].

$$w_M^j = \frac{t_M^{j\,2}}{2G_M^j E_M^j} \qquad \ldots (55)$$

where E_M^j is the stiffness associated with material j and mode M. This localisation limiter is considered a material property and is not to be confused with the characteristic element length. It was assumed that the characteristic length of the mode I transverse crack band mechanism of T800/3900-2 and IM7/8552 were comparable. Thus, Equation (55) was used to calculate G_{IC}^{m} (tabulated in Table 2) by calculating w_M^j using the values for IM7/8552[49] and assuming for $t_{IC}^{m} = E_{22}Y_{\varepsilon T}$ for T800/3900-2.

Since numerous parameters used in simulations of the CNPs were calibrated, a sensitivity study was performed to asses the influence of these parameters on the overall response of these centrally-notched laminates. Both the failure strains and fracture toughnesses were reduced by 20% and the pertinent measures (the splitting load for the (0°) panel, ε_{yy}: the strain in Sg-1 at the splitting load, and the ultimate load for the $(45°/0°/–45°/0°/90°)_s$ panel) were compared to the baseline loads obtained using the values in Table 2. The results of these analyses are tabulated in Tables 3-5.

Table 3 presents the results when the critical strains are reduced by 20%, Table 4 displays the pertinent loads obtained when the fracture toughnesses are reduced by 20%, and Table 5 shows the loads when both the critical strains and fracture toughnesses are reduced by 20%. The ultimate load of the quasi-isotropic laminate, with a centrally located, radiused notch is only

Table 3
Sensitivity of CNP results to changes in critical strains

$X_{\varepsilon T}$	$Y_{\varepsilon T}$	Z_{ε}	Splitting Load (ε_{yy}) (0°)	Ultimate Load $(45°/0°/-45°/0°/90°)_S$
0·021	0·0092	0·0075	36·5kN (621με)	66·8kN
0·0168	0·0092	0·0075	36·5kN (621με)	63·3kN
0·021	0·00736	0·0075	36·5kN (621με)	66·6kN
0·021	0·0092	0·006	33·5kN (557με)	66·6kN

https://doi.org/10.1017/S0001924000007612 Published online by Cambridge University Press

Table 4
Sensitivity of CNP results to changes in fracture toughnesses

			Splitting Load (ε_{yy}) (0°)	Ultimate Load $(45°/0°/–45°/0°/90°)_S$
180 $\frac{kJ}{mm^2}$	0·42 $\frac{kJ}{mm^2}$	1·19 $\frac{kJ}{mm^2}$	36·5kN (621με)	66·8kN
144 $\frac{kJ}{mm^2}$	0·42 $\frac{kJ}{mm^2}$	1·19 $\frac{kJ}{mm^2}$	36·5kN (621με)	58·6kN
180 $\frac{kJ}{mm^2}$	0·33 $\frac{kJ}{mm^2}$	1·19 $\frac{kJ}{mm^2}$	36·5kN (621με)	66·7kN
180 $\frac{kJ}{mm^2}$	0·42 $\frac{kJ}{mm^2}$	0·95 $\frac{kJ}{mm^2}$	33·3kN (581με)	66·8kN

Table 5
Sensitivity of CNP results to changes in critical strains and fracture toughnesses

X_T/G^f_{IC}	Y_T/G^m_{IC}	Y_T/G^m_{IIC}	Splitting Load (ε_{yy}) [0°]	Ultimate Load $[45°/0°/–45°/0°/90°)_S$
0·021/180 $\frac{kJ}{mm^2}$	0·0092/0·42 $\frac{kJ}{mm^2}$	0·0075/1·19 $\frac{kJ}{mm^2}$	36·5kN (621με)	66·8kN
0·0168/144 $\frac{kJ}{mm^2}$	0·0092/0·42 $\frac{kJ}{mm^2}$	0·0075/1·19 $\frac{kJ}{mm^2}$	36·5kN (621με)	60·0kN
0·021/180 $\frac{kJ}{mm^2}$	0·00736/0·33 $\frac{kJ}{mm^2}$	0·0075/1·19 $\frac{kJ}{mm^2}$	36·5kN (621με)	66·5kN
0·021/180 $\frac{kJ}{mm^2}$	0·0092/0·42 $\frac{kJ}{mm^2}$	0·006/0·95 $\frac{kJ}{mm^2}$	30·7kN (532με)	66·6kN

sensitive to change in the axial parameters. A 20% reduction in the critical axial strain, mode I fibre fracture toughness, and both critical strain and fracture toughness yielded to a 10%, 5%, and 12% reduction in the ultimate load of the panel, respectively. Conversely, the unidirectional CNP was only sensitive to changes shear failure parameters. Decreasing the critical shear strain, mode II matrix fracture toughness, and both critical strain and toughness lowered the splitting load of the (0°) CNP by 9%, 9%, and 16%, respectively. Changes in the transverse failure parameters (transverse critical strain and mode I matrix fracture toughness) did not significantly affect the performance of either CNP. It should be noted that these sensitivity results are only valid for these particular lay-ups containing a narrow, centrally located notch. The sensitivity of other lay-ups and/or other configurations on the parameters cannot be inferred from this study.

4.0 CONCLUSIONS

A thermodynamically-based, work potential theory for progressive damage and failure in composite materials, referred to as enhanced Schapery theory, was developed. A marked distinction between damage (pre-peak nonlinearity) and failure (post-peak nonlinearity) was

https://doi.org/10.1017/S0001924000007612 Published online by Cambridge University Press

introduced. Separate internal state variables (ISVs) were used to account for damage and three in-plane failure mechanisms.

In EST, matrix microdamage, which includes matrix microcracking, shear banding, and microvoid growth, is responsible for all damage in a composite lamina and was accounted for with a single ISV, along the lines of the original Schapery theory formulation. The relationship between the transverse and shear moduli of the lamina were related to the ISV through a pair of experimentally-obtainable microdamage functions.

Three major, in-plane failure mechanisms applicable to continuous fibre-reinforced, laminated, polymer matrix composites were identified: mode I matrix cracks, mode II matrix cracks, and fibre breakage. A failure initiation criterion was used to mark the transition from a damaging continuum to a damaged continuum with an embedded discontinuity. After failure initiation, microdamage evolution ceases and separate ISVs are introduced to incorporate the effects of the three major failure mechanisms. Evolution of the failure ISVs is based upon traction-separation laws (which are a functions of the appropriate fracture toughnesses) and a characteristic element length. Typically, the existence of a non-positive definite stiffness tensor would result in pathologically mesh dependent solutions; however, in EST, mesh objectivity is ensured by incorporating a characteristic length scale into the failure evolution.

Experimental results from a center-notched, quasi-isotropic laminate composed of T800/3900-2, and tested under tensile loading at NASA LaRC was used to validate the model findings. Global load versus displacement and global load versus local strain gauge strain data were compared to results obtained from the FEM models utilising EST. Quantitatively, very good correlation was achieved. Furthermore, damage and failure paths predicted by the models matched well with the experimental results.

Since the failure parameters used in the simulations were calibrated or inferred rather than measured, a sensitivity study was performed to asses the influence of these parameters on the response of a unidirectional and quasi-isotropic centrally notched laminates. The critical strains, fracture toughnesses, and both critical strains and fracture toughnesses were reduced by 20%. The splitting load of unidirectional laminate was only affected by the mode II matrix failure parameters, and the ultimate load of the quasi-isotropic laminate was only sensitive to the fibre failure parameters. Neither panels showed any sensitivity to the mode I matrix failure parameters.

Future effort will focus on implementing mixed-mode fracture theories into EST, coupling the evolution of the failure parameters. Additionally, EST can be reformulated to retain the continuum strains after failure has initiated. Finally, a full set of experiments to fully characterise the EST model needs to be performed. The inputs provided from those experiments must be used to predict the response of additional specimens to arrive at a fully-validated model.

REFERENCES

1. LAMBORN, M.J. and SCHAPERY, R.A. An investigation of deformation path-independence of mechanical work in fiber-reinforced plastics, Proceedings of the Fourth Japan-US Conference on Composite Materials, Technomic Publishing Co, Lancaster, PA, USA, 1988.
2. SCHAPERY, R.A. Mechanical characterization and analysis of inelastic composite laminates with growing damage, Mechanics & Materials Center Report5762-89-10, Texas A & M University, College Station, TX 77804, 1989.
3. SCHAPERY, R.A. A theory of mechanical behaviour of elastic media with growing damage and other changes in structure, *J Mech Phys Solids*, **38**, (2), 1990, pp 1725–1797.

https://doi.org/10.1017/S0001924000007612 Published online by Cambridge University Press

4. LAMBORN, M.J. and SCHAPERY, R.A. An investigation of the existence of a work potential for fiberre-inforced plastic, *J Compos Mater*, 1993, **27**, pp 352–382.
5. SICKING, D.L. Mechanical Characterization of Nonlinear Laminated Composites with Transverse Crack Growth, Ph.D. thesis, Texas A&M University, College Station, TX, USA, 1992.
6. SCHAPERY, R.A. and SICKING, D.L. *A Theory Of Mechanical Behaviour Of Elastic Media With Growing Damage And Other Changes In Structure*, *Mechanical Behaviour of Materials*, edited by BAKKER, A. Delft University Press, Delft, The Netherlands, 1995, pp 45–76.
7. BAZANT, Z. and CEDOLIN, L. Blunt crack band propagation in finite element analysis, *J Eng Mech Div.-ASCE*, 1979, **105**, pp 297–315.
8. PIETRUSZCZAK, S. and MROZ, Z. Finite element analysis of deformation of strain-softening materials, *Int J Numer Methods Eng*, 1981, **17**, pp 327–334.
9. PINEDA, E.J., WAAS, A.M., BEDNARCYK, B.A. and COLLIER, C.S. Computational implementation of a thermodynamically based work potential model for progressive microdamage and transverse cracking in fiber-reinforced laminates, 51st AIAA/ASME/ASCE/AHS/ASC Structures, Structural Dynamics, and Materials Conference, Orlando, FL, USA, 12-15 April 2010.
10. BAZANT, Z.P. and OH, B.H. Crack band theory for fracture of concrete, *Mater and Struct*, 1983, **16**, pp 155–77.
11. DE BORST, R. and NAUTA, P. Non-orthogonal cracks in a smeared finite element model, *Eng Comput*, 1985, **2**, pp 35–46.
12. TALREJA, R. A continuum mechanics characterization of damage in composite materials, *P. Roy. Soc. Lond. A Mat*, 1985, **4**, pp 335–375.
13. DVORAK, G.J., LAWS, N. and HEJAZI, M. Analysis of progressive matrix cracking in composite laminates I. Thermoelastic properties of a ply with cracks, *J Compos Mater*, 1985, **19**, pp 216–234.
14. ALLEN, D.H., HARRIS, C.E. and GROVES, S.E. A thermomechanical constitutive theory for elastic composites with distributed damage I. Theoretical development, *Int J Solids Struct*,1987, **23**, (9), pp 1301–1318.
15. LEMAITRE, J. and CHABOCHE, J.-L. *Mechanics of Solid Materials*, Cambridge University Press, 1994.
16. MCCARTNEY, L.N. Predicting transverse crack formation in cross-ply laminates, *Compos Sci Technology*, 1998, **58**, pp 1069–1081.
17. TALREJA, R. (ed), *9 of Composite Materials Series*, Elsevier Science B.V., Amsterdam, The Netherlands, 1994.
18. MATZENMILLER, A., LUBLINER, J. and TAYLOR, R.L. A constitutive model for anisotropic damage in fiber composites, *Mech Mater*, 1995, (20), **2**, pp 125–152.
19. BEDNARCYK, B.A., ABOUDI, J. and ARNOLD, S.M. Micromechanics modelling of composites subjected to multiaxial progressive damage in the constituents, *AIAA J*, 2010, **48**, pp 1367–1378.
20. PINEDA, E.J. A Novel Multiscale Physics-Based Progressive Damage and Failure Modelling Tool for Advanced Composite Structures, Ph.D. thesis, Universtiy of Michigan, Ann Arbor, MI, USA, 2012.
21. PINEDA, E.J. and WAAS, A.M. Numerical implementation of a multiple-ISV thermodynamicallybased work potential theory for modelling progressive damage and failure in fiber-reinforced laminates, NASA/TM 2011-217401, 2011.
22. BOGERT, P.B., SATYANARAYANA, A. and CHUNCHU, P.B. Comparison of damage path predicions for composite laminates by explicit and standard finite element analysis tool, 47 AIAA Structures, Structural Dynamics, and Materials Conference, 1-4 May 2006.
23. SATYANARAYANA, A., BOGERT, P. B. and Chunchu, P. B. The effect of delamination on damage path and failure load prediction for notched composite laminates, 48th AIAA Structures, Structural Dynamics, and Materials Conference, 23-26 April 2007.
24. SCHAPERY, R.A. Prediction of compressive strength and kink bands in composites using a work potential, *Int J Solids Structures*, 1995, **32**, (6), pp 739–765.
25. BASU, S., WAAS, A.M. and AMBUR, D.R. Prediction of progressive failure in multidirectional composite laminated panels, *Int J Solids Structures*, 2007, **44**, (9), pp 2648–2676.
26. PINEDA, E.J., WAAS, A.M., BEDNARCYK, B.A., COLLIER, C.S. and YARRINGTON, P.W. Progressive damage and faiure modelling in notched laminated fiber reinforced composites, *Int J Fract*, 2009, **158**, pp 125–143.
27. HINTERHOELZL, A. and SCHAPERY, R.A. FEM implementation of a three-dimensional visoelastic constitutive model for particulate composites with damage growth, *Mech Time-Depend Mat*, 2004, **8**, 1, pp 65–94.

28. RICE, J.R. Inelastic constitutive relations for solids: an internal-variable theory and its application to metal plasticity, *J Mech Phys Solids*, **19**, 1971, pp 433–455, bon fiber composites, *J Compos Mater*, 2006, **40**, (22).
29. HASHIN, Z. and ROTEM, A. A fatigue failure criterion for fiber reinforced composite materials, *J Composite Materials*, 1973, **7**, pp 448–464.
30. DUGDALE, D.S. Yielding of steel sheets containing slits, *J Mech Phys Solids*, 1960, **8**, pp 100–108.
31. BARENBLATT, G.I. The mathematical theory of equilibrium cracks in brittle fracture, *Adv Appl Mech*, **7**, 1962, pp 55–129.
32. GUSTAFSON, P.A. and WAAS, A.M. The influence of adhesive constitutive parameters in cohesive zone finite element models of adhesively bonded joints, *Int J Solids Struct*, 2009, pp 2201–2215.
33. ORTIZ, M. and PANDOLFI, A. Finite-deformation irreversible cohesive elements for three dimensional crack-propagation analysis, *Int J Numer Meth*, 1999, **44**, pp 1267–1282.
34. CAMANHO, P.P. and DÁVILA, C.G. Mixed-mode decohesion finite elements for the simulation of delamination in composite materials, NASA/TM 2002-211737, 2002.
35. XIE, D.E., SALVI, A., SUN, C.E., WAAS, A.M. and CALISKAN, A. Discrete cohesive zone model to simulate static fracture in 2-D triaxially braided carbon fiber composites, *J Compos Mater,* 2006, **40**, (22).
36. GUSTAFSON, P.A. Analytical and Experimental Methods for Adhesively Bonded Joints Subjected to High Temperatures, PhD. thesis, University of Michigan, Ann Arbor, MI, USA, 2008.
37. TURON, A., CAMANHO, P.P., COSTA, J. and DAVILA, C.G. A damage model for the simulation of delamination in advanced composites under variable-mode loading, *Mech Mater*, 2006, **38**, (11).
38. RANATUNGA,V., BEDNARCYK, B.A. and ARNOLD, S.M. Modelling progressive damage using local displacement discontinuities with the FEAMAC multiscale modelling framework, NASA/TM 2010-216825, 2010.
39. BUDIANSKY, B. and FLECK, N.A. Compressive failure of fiber composites, *J Mech Phys Solids*, 1993, **41**, (1), pp 183–211.
40. BASU, S., WAAS, A.M. and AMBUR, D.R. Compressive failure of fiber composites under multiaxial loading, *J Mech Phys Solids*, 2006, **54**, (3), pp 611–634.
41. HOEK, E. and BIENIAWSKI, Z.T. Brittle rock fracture propagation in rock under compression, *Int J Fract*, 1965, **1**, (3), pp 137–155.
42. PUCK, A. and SCHÜRMANN, H. Failure analysis of FRP laminates by means of physically based phenomenological models, *Comps Sci Technol*, 1998, **58**, pp 1045–1067.
43. LIECHTI, K. and HANSON, E. Non-linear effects in mixed-mode interfacial delaminations, *Int J Fract*, 1988, **36**, pp 199–217.
44. BENZEGGAGH, M. and KENANE, M. Measurement of mixed-mode delamination fracture toughness of unidirectional glass/epoxy composites with mixed-mode bending apparatus, *Compos Sci Technol*, 1996, **56**, pp 439–449.
45. BAŽANT, Z.P. Crack band model for fracture of geomaterials, Proceedings of the 4th International Conference on Numerical Methods in Geomechanics, Edmonton, Canada, 1982.
46. ROTS, J.G. and DE BORST, R. Analysis of mixedmode fracture in concrete, *J Eng Mech*, 1987, **113**, (11), pp 1739–1758.
47. ABAQUS, Abaqus User's Manual,1-3, Version 6.10-1, Dassault Systemes Simulia Corp, Providence, RI, USA, 2008.
48. BASU, S. Computational Modelling of Progrssive Failure and Damage in Composite Laminates, PhD. thesis, University of Michigan, Ann Arbor, MI, USA, 2005.
49. CAMANHO, P.P., DÁVILA, C.G., PINHO, S.T., IANNUCCI, L. and ROBINSON, P. Prediction of in situ strenghts and matrix cracking in composites under transverse tension and in-plane shear, Composites: Part A, 2006, **37**, pp 165–176.